Highly porous polyimide-derived carbon aerogel as advanced three-dimensional framework of electrode materials for high-performance supercapacitors

Youfang Zhang [a, b], Wei Fan [a, **], Hengyi Lu [b], Tianxi Liu [a, b, *]

[a] State Key Laboratory for Modification of Chemical Fibers and Polymer Materials, College of Materials Science and Engineering, Donghua University, 2999 North Renmin Road, Shanghai 201620, PR China
[b] State Key Laboratory of Molecular Engineering of Polymers, Department of Macromolecular Science, Fudan University, 220 Handan Road, Shanghai 200433, PR China

ABSTRACT

The hybridization of highly porous carbon materials and battery-type materials is an effective method for achieving supercapacitors with both high energy density and good rate capability. The structure of the carbon substrate should be carefully designed to meet the requirement of good conductivity and good accessibility to electrolyte and ions. In this work, graphene nanoribbon crosslinked polyimide-derived carbon aerogels (a-GCA) with hierarchical porous structures and large specific surface area of 2413.0 $m^2 g^{-1}$ have been first constructed, and then applied as a conductive template for the uniform growth of ultrathin Ni(OH)$_2$ nanosheets. In the obtained Ni(OH)$_2$/a-GCA hybrids, a-GCA can provide open and interconnected channels for rapid diffusion of ions and electrons to access Ni(OH)$_2$ nanosheets for fast Faradaic redox reactions, as well as enhance the stability of Ni(OH)$_2$ nanosheets. Consequently, the optimized Ni(OH)$_2$/a-GCA hybrid exhibits a high specific capacitance of 537.0 $C g^{-1}$ at a charge/discharge current density of 1 $A g^{-1}$, excellent rate capacitance retention of 78.4% at 10 $A g^{-1}$. Moreover, the assembled Ni(OH)$_2$/a-GCA//a-GCA hybrid supercapacitor device delivers a high energy density of 54.8 Wh kg^{-1} at a powder density of 816 $W kg^{-1}$. Therefore, the Ni(OH)$_2$/a-GCA hybrid shows great potential as high-performance electrode materials in applications in energy storage device.

© 2018 Elsevier Ltd. All rights reserved.

1. Introduction

Supercapacitors with super-fast charge/discharge capability, high power density, and long cycle life show great potentials in portable electronic devices, electric vehicles, and many other energy fields. Supercapacitors work based on two kinds of mechanisms: electrical double-layer capacitors and electrochemical pseudocapacitors [1,2]. Specially, electrical double-layer capacitors store energy by reversible physical absorption/desorption at the electrode/electrolyte (solid/liquid) interface, while pseudocapacitors store energy via surface redox reactions. Based on these energy storage mechanisms, pseudocapacitors exhibit higher charge storage than electrical double-layer capacitors. However, both these two supercapacitors have low energy density, which hampers their practical applications. To feasibly and effectively address these issues, hybrid supercapacitors with an electrical double-layer capacitor or pseudocapacitive type electrode and a battery-type material have been proposed [3,4].

As typical electrical double-layer capacitor materials, carbon nanomaterials, such as graphene, carbon nanotubes (CNTs), carbon nanofibers, activated carbon, and carbon aerogels have been extensively explored due to their excellent conductivity and stability [5,6]. Moreover, these carbon nanomaterials are usually investigated as ideal substrates for loading electrochemically active nanomaterials due to their large surface area and good compatibility. Among them, carbon aerogels with three-dimensional (3D) interconnected carbon skeleton, high porosity, large surface area, and good conductivity, are often applied as electrical double-layer capacitor materials and promising substrates [7,8]. Generally,

* Corresponding author. State Key Laboratory for Modification of Chemical Fibers and Polymer Materials, College of Materials Science and Engineering, Donghua University, 2999 North Renmin Road, Shanghai 201620, PR China.
** Corresponding author.
E-mail addresses: weifan@dhu.edu.cn (W. Fan), txliu@dhu.edu.cn, txliu@fudan.edu.cn (T. Liu).

carbon aerogels can be divided into three kinds based on the raw material source. One is derived from carbon nanomaterials like graphene, CNTs, graphene nanoribbons, and their hybrids [9–13]. The second one is derived from biomass-based materials, such as cotton, watermelon, bacterial cellulose, and so on [14–16]. The third one is derived from polymer-based aerogels [17–19]. Compared with carbon aerogels derived from carbon nano-materials and biomass-based materials, the structure of carbon aerogels derived from polymer-based aerogels can be easily adjusted by varied polymers. Recently, polyimide aerogels derived carbon aerogels have been developed due to eco-friendly fabrication, high production of carbon and easily adjustable morphologies. For instance, in our previous report, graphene/polyimide-derived carbon aerogels with hierarchical porous structures (*e.g.*, macro, meso or microporous structure) were fabricated, and applied as electrical double-layer capacitor materials, as well as good sub-strates for the growth of nanoparticles [17,20]. Besides, we have showed that graphene oxide (GO) and KOH activation can greatly affect the morphology, specific surface area and capacitance of polyimide-derived carbon aerogels [21]. Apart from GO, graphene oxide nanoribbons (GONR) derived from unzipping pristine CNTs also have abundant oxygen-containing functional groups, which may react with the water-soluble polyimide precursor, *i.e.*, poly(a-mic acid) (PAA) in sol-gel process and act as crosslinking and pore-forming agents. Moreover, the unique aspect ratio of GONR offers more chances to crosslink with PAA, thus forming conductive interconnected network. Therefore, GONR with abundant functional groups and unique aspect ratio is expected to be an effective crosslinking and pore-forming agent for preparation of carbon aerogels with hierarchical porous structure and high surface area.

Transition metal oxides [22,23], hydroxides [24,25], sulfides [26], layered double hydroxides [27,28], and nitrides [29–32] have been widely applied as battery-type materials because of their faradic reactions. In particular, $Ni(OH)_2$ nanosheets with low cost, non-toxicity and high redox activity endow them as ideal electrode materials for hybrid supercapacitors. For instance, Elshahawy et al. [33] successfully prepared nanocrystalline β-$Ni(OH)_2$ powder with a high specific capacitance of $1566\,F\,g^{-1}$ at $1\,A\,g^{-1}$ in 6 M KOH electrolyte. Du et al. [34] fabricated $Ni(OH)_2$ microspheres composed of intercalated nanopetals by a facile hydrothermal method. The optimized $Ni(OH)_2$ microspheres with macro/meso-porous structure display high specific capacitance of $1280.9\,F\,g^{-1}$ at $0.5\,A\,g^{-1}$ and $655.2\,F\,g^{-1}$ at $10\,A\,g^{-1}$ in 2 M KOH electrolyte. However, $Ni(OH)_2$ fabricated in the form of agglomerates usually suffers from limited specific surface area, large volumetric expansion and poor conductivity, resulting in poor electrochemical performance, especially poor rate and cycling stability. To overcome these issues, one simple and effective approach is to confine $Ni(OH)_2$ on a conductive carbonaceous substrate with large specific surface area [35–37]. Hybridization $Ni(OH)_2$ with proper carbonaceous sub-strate could not only incorporate electrical double-layer capacitor capacitance but also maximize the utilization of electrochemically active $Ni(OH)_2$, meanwhile providing better stability and rate per-formance [38–41]. Therefore, the structure and property of carbon substrate need to be carefully designed and tailored to optimize the performance of hybrid supercapacitors.

Herein, KOH-activated graphene nanoribbon enhanced polyimide-derived carbon aerogels (a-GCA) with controllable hi-erarchical structures and super-large specific surface area have been first constructed by carbonization of KOH-GONR/PI aerogel. Subsequently, a-GCA is applied as a 3D template for the uniform growth of ultrathin $Ni(OH)_2$ nanosheets. For the obtained $Ni(OH)_2$/a-GCA hybrids, a-GCA with high porosity offer abundant sites for in-situ growth of $Ni(OH)_2$ nanosheets to prevent their self-aggregation, maximizing the exposure of active edge sites of $Ni(OH)_2$. Moreover, 3D interconnected and continuous carbon backbone of a-GCA can provide a lot of channels for rapid diffusion of ions and electrons to access the electrochemically active $Ni(OH)_2$ nanosheets for fast Faradaic redox reactions, which can improve the conductivity and enhance the rate capability of the electrode. Additionally, the porous structure of a-GCA can buffer the volu-metric expansion/contraction of $Ni(OH)_2$ nanosheets during the long-term cycle and improve the stability of $Ni(OH)_2$ nanosheets. Consequently, the optimized $Ni(OH)_2$/a-GCA hybrid shows a high specific capacitance of $537.0\,C\,g^{-1}$ at a charge/discharge current density of $1\,A\,g^{-1}$ and excellent rate capacitance retention of 78.4% at $10\,A\,g^{-1}$. Moreover, a hybrid supercapacitor based on $Ni(OH)_2$/a-GCA//a-GCA shows a high energy density of $54.8\,Wh\,kg^{-1}$ at a powder density of $816\,W\,kg^{-1}$. Therefore, $Ni(OH)_2$/a-GCA hybrids with such an excellent electrochemical capacitance can be regarded as promising electrode materials for hybrid supercapacitors.

2. Experimental section

2.1. Materials

4,4'-oxidianiline, pyromellitic dianhydride, triethylamine (99%), *N, N*-dimethylacetamide, 98% H_2SO_4, 30% H_2O_2, $KMnO_4$, 37% HCl, 85% H_3PO_4, KOH, nickel (ii) nitrate hexahydrate, and urea were commercially purchased from Sinopharm Chemical Reagent Co., Ltd. Multi-walled CNTs (diameter of 20–40 nm) were obtained from Chengdu Organic Chemicals Co. Ltd. Deionized water was used as the solvent throughout the experiments. All chemicals were used as received.

2.2. Preparation of a-GCA

GONR was prepared from pristine CNTs according to solution oxidation method [42–44]. The well exfoliated GONR suspension with $8\,mg\,mL^{-1}$ was prepared by ultrasonicating GONR powder in deionized water for further use. Briefly, 1 g water-soluble PAA and 0.5 g triethylamine were dissolved in 10 mL GONR suspension un-der continuous stirring for 30 min. Then 1 mL KOH solution with the concentration of $0.5\,g\,mL^{-1}$ was quickly added into the above GONR/PAA solution and kept stirring for 30 min. After homoge-neously mixed, the KOH-GONR/PAA solution was transferred into a cylindrical mold for gelation to form KOH-GONR/PAA hydrogel. Subsequently, the hydrogel was frozen and dried in a lyophilizer to form KOH-GONR/PAA aerogel. KOH-GNR/PI aerogel could be ob-tained by completely thermal imidization of KOH-GONR/PAA aer-ogel. Finally, a-GCA was obtained by high temperature carbonization at 800 °C in nitrogen atmosphere for 4 h, during which the KOH activation and GONR reduction occurred.

2.3. Preparation of Ni(OH)₂/a-GCA hybrids

The $Ni(OH)_2$/a-GCA hybrids with different loading amounts of $Ni(OH)_2$ were synthesized by a chemical bath deposition method as schematically shown in Fig. 1. Typically, 0.5 mmol $Ni(NO_3)_2 \cdot 6H_2O$ and 5 mmol urea were dissolved in DI water and ethanol (volume ratio of 1:1) via continuous stirring. Then, certain amount of a-GCA (a-GCA was first ball-milled at 500 rpm for 2 h before use) was immersed into the above solution and heated up to 70 °C in a water bath for 6 h. After naturally cooled down to room temperature, the obtained hybrid was washed with DI water and centrifuged for three times, and dried at 80 °C to collect $Ni(OH)_2$/a-GCA-0.5 hybrid. Additionally, $Ni(OH)_2$/a-GCA-1 and $Ni(OH)_2$/a-GCA-2 hybrids were prepared with the same procedures by changing the mole weight of $Ni(NO_3)_2 \cdot 6H_2O$. For comparison, pure $Ni(OH)_2$ nanosheets were synthesized under the same conditions without adding a-GCA template.
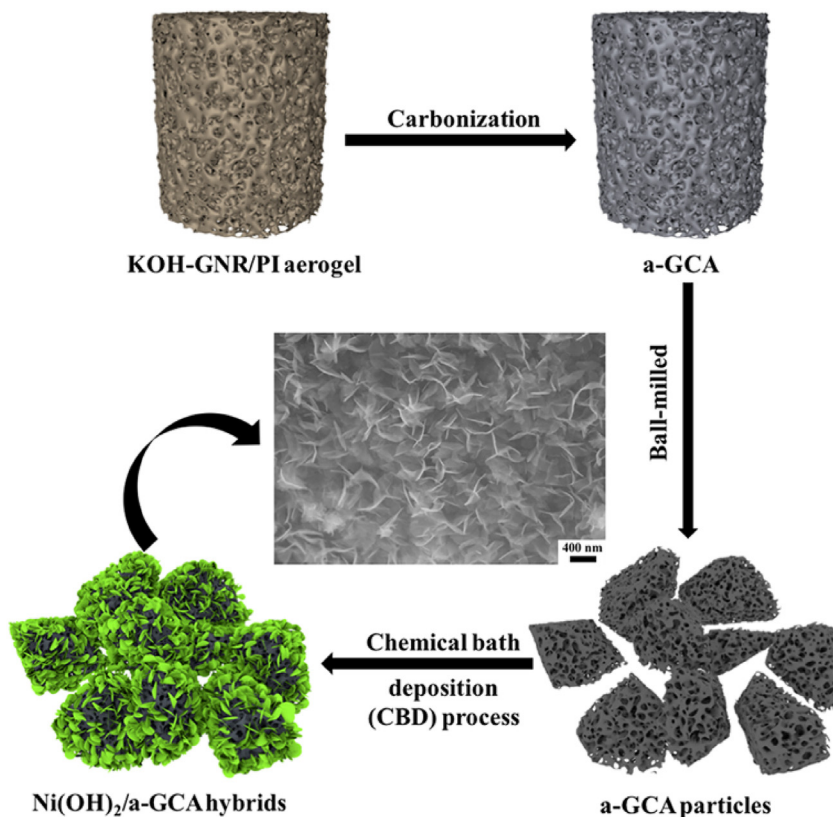
Fig. 1. Schematic illustration of the preparation of Ni(OH)$_2$/a-GCA hybrids.

2.4. Characterization

The structures and morphologies of the as-prepared samples were investigated by a field emission scanning electron microscopy (FESEM) (Ultra 55, Zeiss) at an acceleration voltage of 5 kV and the chemical composition was investigated by the energy dispersive X-ray spectroscopy (EDX). Moreover, the samples after cyclic test were observed by FESEM. Transmission electron microscopy (TEM) was performed on a Tecnai G2 TWIN TEM for Ni(OH)$_2$/CA-1 hybrid. X-ray diffraction (XRD) patterns were conducted from $2\theta = 5°$ to 80° on an X'Pert Pro X-ray diffractometer with CuKα radiation ($\lambda = 0.1542$ nm) under a voltage of 40 kV and a current of 40 mA. The data of X-ray photoelectron spectroscopy (XPS) were collected on a device of VG ESCALAB 220I-XL. All XPS spectra were corrected using C 1s line at 284.5 eV. Thermogravimetric analysis (Pyris 1 TGA) was performed under air flow from 100 to 800 °C at a heating rate of 20 °C min^{-1}. The specific surface area and pore size distribution was performed with a belsorp-max surface area detecting instrument (Tristar 3000) by N$_2$ physisorption at 77 K.

2.5. Electrochemical measurements

The electrochemical properties of all the samples were investigated in a typical three-electrode cells by using a CHI 660D electrochemical workstation (Chenhua Instruments Co, Shanghai, China). In this three-electrode system, Pt wire was used as a counter electrode, Hg/HgO was applied as a reference electrode. Working electrodes were prepared as follows: the obtained electrode materials was first mixed with 10% polyvinylidene fluoride and 10% carbon black using isopropanol as solvent to form homogeneous slurry. Then the slurry was coated onto carbon paper and dried at 80 °C for 12 h, and further pressed under 10 Mpa for 30 s.

Cyclic voltammetry (CV), galvanostatic charge/discharge curves, electrochemical impedance spectroscopy (EIS) measurements and cycling tests were all carried out in 2 M KOH solution at room temperature. EIS was recorded in the frequency range from 0.01 Hz to 100 kHz at an open circuit potential with amplitude of 5 mV. For the three-electrode configuration, the specific capacitance (C, C g^{-1}) was calculated from the discharge part of the galvanostatic charge/discharge curves according to the formula:

$$C = I \, \Delta t / m \tag{1}$$

where I (A) is the discharge current, Δt (s) is the discharge time, and m (g) is the mass of the active materials.

The hybrid supercapacitor was assembled by using Ni(OH)$_2$/a-GCA hybrids as positive electrode materials and a-GCA as negative material. The mass ratio of Ni(OH)$_2$/a-GCA hybrids to a-GCA was set according to their specific capacitances obtained from the three-electrode system, using the following formula:

$$m_+/m_- = C_- \times \Delta V_-/C_+ \tag{2}$$

where m (g) is the mass of the electrode materials, C_+ (C g^{-1}) is the specific capacitance of positive electrode, C_- (F g^{-1}) is the specific capacitance of negative electrode, and ΔV_- is the potential range of negative electrode during charge-discharge process.

The energy density (E, Wh kg^{-1}) and power density (P, W kg^{-1}) was evaluated using the following equations:

$$E = \frac{1}{2} \times C \times V \tag{3}$$

$$P = E/\Delta t \qquad (4)$$

where C (C g^{-1}) is the specific capacitance, V (V) is the potential window, Δt (s) is the discharge time.

3. Results and discussion

3.1. Structures and morphology of Ni(OH)$_2$/a-GCA hybrids

GONR with straight edges was simply fabricated by longitudinally unzipping pristine CNTs according to the previous report (Fig. S1a) [42,43]. As indicated in the XRD patterns (Fig. S1b), GONR shows a very different diffraction peak at $2\theta = 11.2°$ compared with pristine CNTs, indicating that pristine CNTs have been completely opened or unzipped by chemical scissors. As shown in Fig. S1c, pristine CNTs with diameters ranging from 20—50 nm exhibit bamboo-like hollow structure and self-aggregate together. In contrast, GONR displays a wide band structure with curly and corrugated edges, and adjacent GONRs are connected with each other to form a 3D networks (Fig. S1d).

The typical morphology of the a-GCA is shown by the SEM images in Fig. 2. The overview SEM image of a-GCA (Fig. 2a) exhibits a 3D porous structure with large pores with diameter of several micrometers. Close observation of the pore walls (Fig. 2b), there are a lot of uniformly distributed honeycomb pores, with sizes of several nanometers. According to the previous report [21], addition of carbon nanomaterials with abundant oxygen-functional groups and KOH activation are efficient method for fabricating CAs with hierarchical porous structures. In this work, GONR with abundant oxygen-containing functional groups can crosslink with PAA in the sol-gel, aging and imidization processes to form a lot of crosslinking

points and fabricate 3D carbon framework with large pores. On the other hand, KOH reacts with carbon element during 400—800 °C and generates a lot of gases (H$_2$, CO and CO$_2$) and metallic potassium or their compounds. After the removal of these gases, K and potassium compounds, abundant mesopores and micropores can be formed on the carbon framework. Besides, the addition of carbon nanomaterials can accelerate the reaction of KOH and carbon, thus forming more pores, since KOH prior reacts with defect-rich carbon. Hence, with the crosslinking effect of GONR and KOH activation, hierarchical porous architecture of a-GCA can be facilely fabricated. The specific surface area of a-GCA obtained from BET analysis is 2413.0 m^2 g^{-1}, indicating that the addition of GONR and KOH activation significantly enhances the specific surface area. It can be seen that the isotherm curve of a-GCA belongs to type IV with a clear hysteresis loop, showing that a-GCA possesses a great many of micropores and mesopores (Fig. 2c). Both micropores and mesopores contribute to enhanced electrochemical performance, where micropores can store more capacity while mesopores can facilitate ion diffusion. The pore size distribution of a-GCA is mainly in the range of 2—20 nm, relatively wide due to reaction sequence of KOH and carbon skeleton (Fig. 2d).

The as-prepared a-GCA with 3D hierarchical porous structures and super-large specific surface area is utilized as substrate for vertically growth of Ni(OH)$_2$ nanosheets. Fig. 3 shows the morphologies of Ni(OH)$_2$/a-GCA hybrids with different loading amounts of Ni(OH)$_2$ nanosheets. It can be clearly seen that the initial amount of nickel salts greatly affects the growth of Ni(OH)$_2$ nanosheets. Ni(OH)$_2$ nanosheets are sparsely grown on the surface of a-GCA for Ni(OH)$_2$/a-GCA-0.5 hybrid and there are a lot of bare surface sites (Fig. 3a and b). With the increase of dosage of initial nickel salt, more and more Ni(OH)$_2$ nanosheets are anchored on the
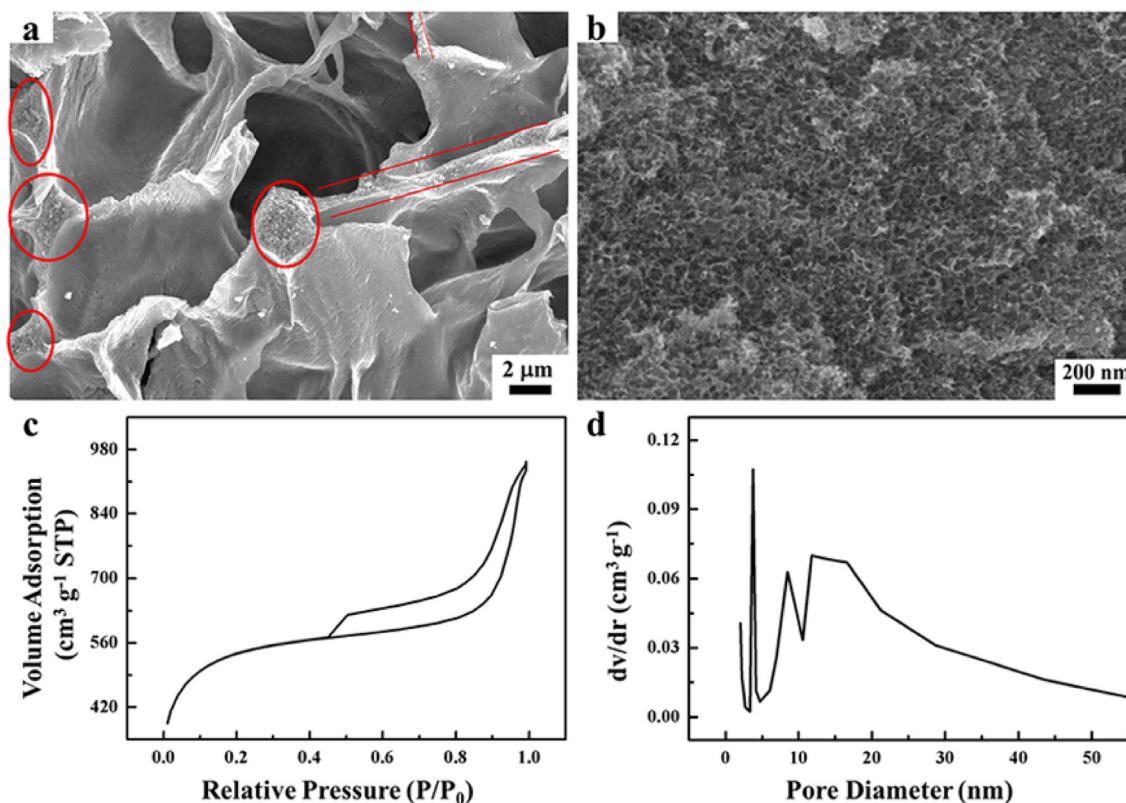

Fig. 2. SEM images of a-GCA at (a) low and (b) high magnifications, (c) N$_2$ adsorption/desorption isotherm of a-GCA at 77 K, (d) pore size distribution as determined by the Barrett-Joynes-Halenda (BJH) method.
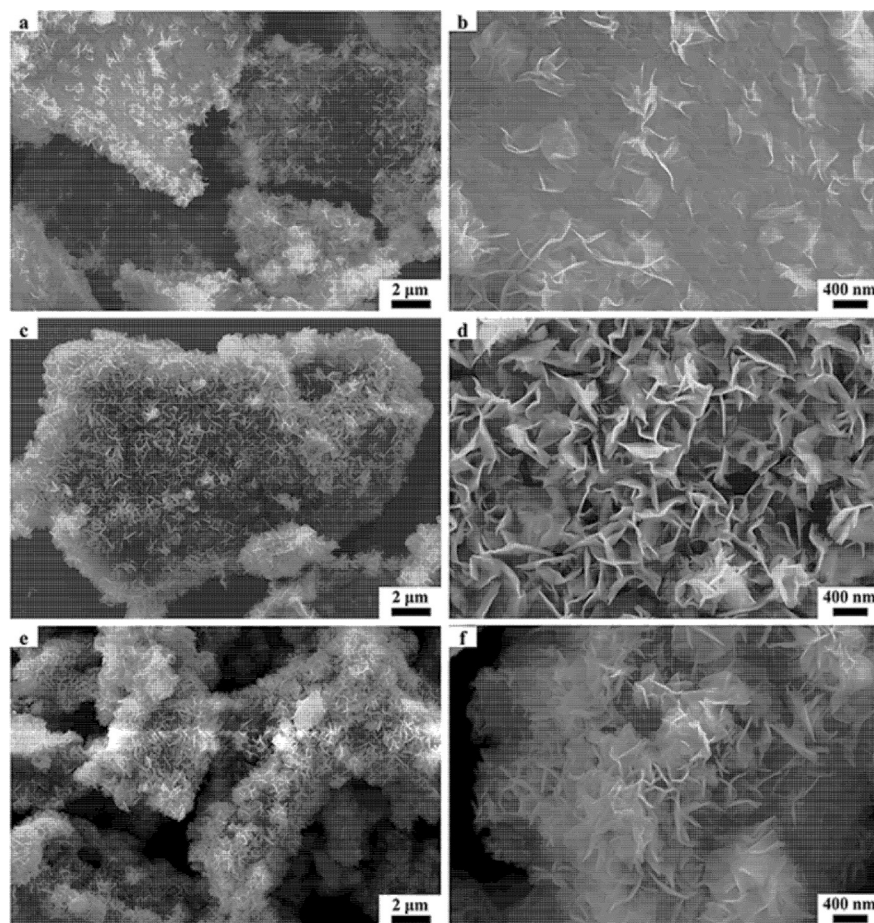
Fig. 3. SEM images of (a, b) Ni(OH)$_2$/a-GCA-0.5, (c, d) Ni(OH)$_2$/a-GCA-1, and (e, f) Ni(OH)$_2$/a-GCA-2 at low (left) and high (right) magnifications.

surface of a-GCA. For Ni(OH)$_2$/a-GCA-1 hybrid, Ni(OH)$_2$ nanosheets are uniformly and fully interspersed on the surface of a-GCA (Fig. 3c and d), while excess Ni(OH)$_2$ nanosheets aggregate into micro-sized spheres on the surface of a-GCA, for example, for Ni(OH)$_2$/a-GCA-2 hybrid (Fig. 3e and f). In the Ni(OH)$_2$/a-GCA-1 hybrid, a-GCA can be completely covered by Ni(OH)$_2$ nanosheets, maximizing the exposure of active edge sites of Ni(OH)$_2$ nanosheets for fast Faradaic reaction. EDX mapping images (Fig. S2) also show coexistence of C, Ni and O elements, with uniform distribution of Ni and O elements, which also confirms that Ni(OH)$_2$ nanosheets are uniformly distributed on the surface of a-GCA. Additionally, the TEM image (Fig. S3) of Ni(OH)$_2$/a-GCA-1 hybrid also reveals that Ni(OH)$_2$ nanosheets are evenly and vertically grown on a-GCA, which is in accordance with the SEM observations. For comparison, pure Ni(OH)$_2$ nanosheets were prepared in the absence of a-GCA. As shown in Fig. S4, pure Ni(OH)$_2$ nanosheets seriously aggregate into large spheres, implying the importance of the highly porous a-GCA template for effectively preventing the aggregation of Ni(OH)$_2$ nanosheets.

The superiority of Ni(OH)$_2$/a-GCA hybrids in pore structure and specific surface area over neat Ni(OH)$_2$ is also evidenced via nitrogen physisorption (Fig. 4). It is obvious that all isotherm curves of Ni(OH)$_2$/a-GCA hybrids belong to IV type with a clear hysteresis loop (Fig. 4a). Specially, the isotherm curves of Ni(OH)$_2$/a-GCA-2 even exhibits clear hysteresis loop at low relative pressure, which means N$_2$ gas hardly comes in and out of Ni(OH)$_2$/a-GCA-2. The specific surface areas of Ni(OH)$_2$/a-GCA-0.5, Ni(OH)$_2$/a-GCA-1, and Ni(OH)$_2$/a-GCA-2 hybrids are 1102.7, 803.4 and 350.6 m^2 g^{-1},

respectively. With the amount of Ni(OH)$_2$ nanosheets increase, the surface area of Ni(OH)$_2$/a-GCA hybrids decreases, indicating that the growth of Ni(OH)$_2$ nanosheets greatly hinders the exposure of surface area. All the hybrids exhibit a narrow pore size distribution centered at 4 nm, indicating mesoporous structures (Fig. 4b). Compared with solid Ni(OH)$_2$ nanosheets, the porous structure of Ni(OH)$_2$/a-GCA hybrids benefits the accessibility of the electrode materials by the electrolyte and fast transport of ions and charges, which will enhance the electrochemical performance.

The loading amount of Ni(OH)$_2$ nanosheets in the Ni(OH)$_2$/a-GCA hybrids is investigated by TGA test. As shown in Fig. 5a, pure Ni(OH)$_2$ nanosheets exhibit one stage of thermal degradation, where the transformation of pure Ni(OH)$_2$ into NiO occurs at the temperature ranging from 330−370 °C. However, all the TGA curves of Ni(OH)$_2$/a-GCA hybrids show two stages of thermal degradation. The first stage is the transformation of Ni(OH)$_2$ into NiO and the second stage is related to the decomposition of a-GCA. Clearly, the temperature gap in the second stage becomes narrow with the amount of Ni(OH)$_2$ increase. As calculated from Fig. 5a, the weight ratios of Ni(OH)$_2$ nanosheets in Ni(OH)$_2$/a-GCA-0.5, Ni(OH)$_2$/a-GCA-1 and Ni(OH)$_2$/a-GCA-2 are 13.0 wt%, 36.0 wt%, and 54.9 wt%, respectively. As observed from the XRD pattern in Fig. 5b, there is a wide diffraction peak at $2\theta = 26°$ and a weak diffraction peak at $2\theta = 44°$ for a-GCA, which are assigned to the (002) and (100) planes of carbon (JCPDS No. 01-0646). The XRD patterns of pure Ni(OH)$_2$ and Ni(OH)$_2$/a-GCA hybrids show peaks centered at $2\theta = 12.8°$, 25.5°, 34.1°, and 60.9°, which can be well indexed to the (003), (006), (101), and (110) planes of α-Ni(OH)$_2$. The diffraction

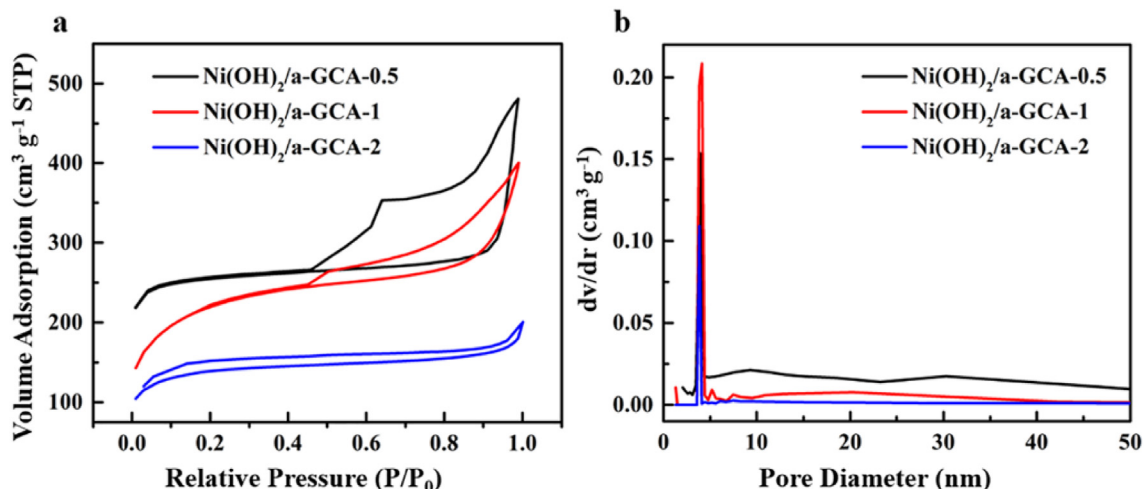**Fig. 4.** (a) N_2 adsorption/desorption isotherm of $Ni(OH)_2$/a-GCA-0.5, $Ni(OH)_2$/a-GCA-1, and $Ni(OH)_2$/a-GCA-2 at 77 K, and (b) pore size distribution as determined by the Barrett-Joynes-Halenda (BJH) method.
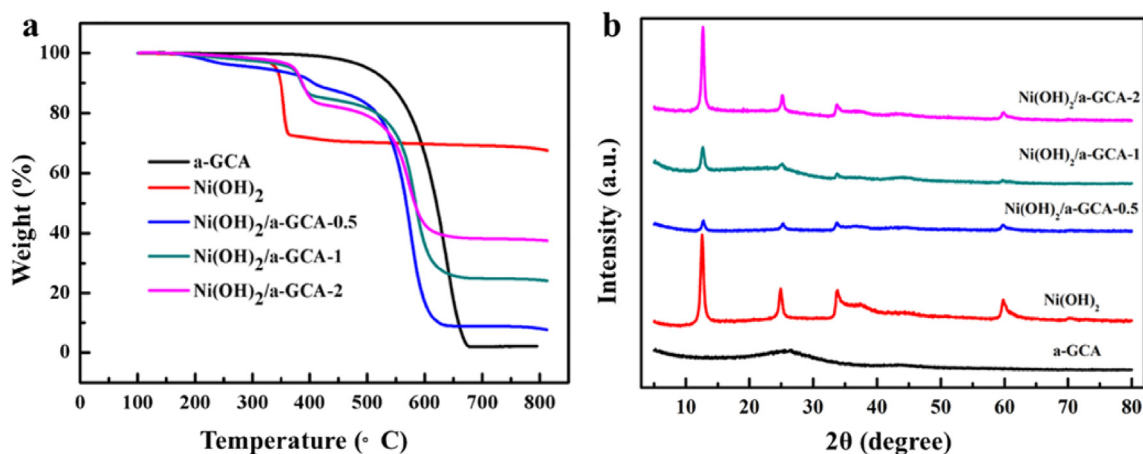

Fig. 5. (a) TGA curves, and (b) XRD patterns of a-GCA, pure $Ni(OH)_2$ and $Ni(OH)_2$/a-GCA hybrids.

peaks of a-GCA in $Ni(OH)_2$/a-GCA hybrids disappear due to strong diffraction of highly crystalline $Ni(OH)_2$, which relatively conceals the diffraction of a-GCA. Besides, the intensity of the typical diffraction peaks gradually enhances from $Ni(OH)_2$/a-GCA-0.5, $Ni(OH)_2$/a-GCA-1 to $Ni(OH)_2$/a-GCA-2, due to the increased loading amount of $Ni(OH)_2$ nanosheets in the hybrids. Thus, the XRD results suggest that $Ni(OH)_2$ nanosheets are successfully grown on the a-GCA template. The chemical elemental states of $Ni(OH)_2$/a-GCA-1 were further studied by XPS spectra. The survey spectrum (Fig. S5a) reveals that C, Ni and O elements co-exist in $Ni(OH)_2$/a-GCA-1 hybrid. High resolution of Ni 2p spectrum (Fig. S5b) exhibits characteristic peaks located at 855.4, 873.3, 861.4, and 879.1 eV corresponding to the binding energies of Ni $2p_{3/2}$, Ni $2p_{1/2}$ and their associated satellite peaks, respectively, suggesting the presence of Ni^{2+} in $Ni(OH)_2$/a-GCA-1 hybrid.

3.2. Electrochemical performance of $Ni(OH)_2$/a-GCA hybrids

Fig. 6a shows the typical CV curves of pure $Ni(OH)_2$ nanosheets and $Ni(OH)_2$/a-GCA hybrids in 2 M KOH solution. It can be clearly seen that all CV curves exhibit a couple of redox peaks in the relative voltage range, showing that all the samples have faradaic behaviors. Based on references [45−48], the related energy storage

mechanism of pure $Ni(OH)_2$ and $Ni(OH)_2$/a-GCA hybrids is mainly associated with the following reversible faradaic redox reaction between $Ni(OH)_2$ and NiOOH in KOH electrolyte:

$$Ni(OH)_2 + OH^- \leftrightarrow NiOOH + H_2O + e^- \qquad (5)$$
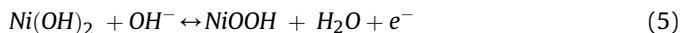
In the anodic scan, electrolyte enter the interval between $Ni(OH)_2$ nanosheets on both outside and inner surface of a-GCA. Thus, OH^- ions react with $Ni(OH)_2$ nanosheets effectively and generate NiOOH, water and negative charges. Inversely, the reversible reaction occurs in the cathodic scan. It is clear that $Ni(OH)_2$/a-GCA-1 hybrid shows the optimized performance for supercapacitors due to the largest area of CV curves. To better understand the differences in the electrochemical behaviors of pure $Ni(OH)_2$ and $Ni(OH)_2$/a-GCA hybrids, rate stabilities are further investigated by analyzing CV curves at various scan rates and galvanostatic charge/discharge curves at different current densities. As shown in Fig. 6b and Fig. S6a−c, the current densities increase and the redox peaks shift to high voltage as the scan rates increase from 2 to 50 mV s^{-1}. It is worthy to note that the shape of CV curves for $Ni(OH)_2$/a-GCA hybrids maintain well and all redox peaks exhibit clearly, indicating a good rate stability. However, the shapes of CV curves for pure $Ni(OH)_2$ (Fig. S6a) deformed and the redox peaks almost disappear at high scan rate of 50 mV s^{-1}, indicating that
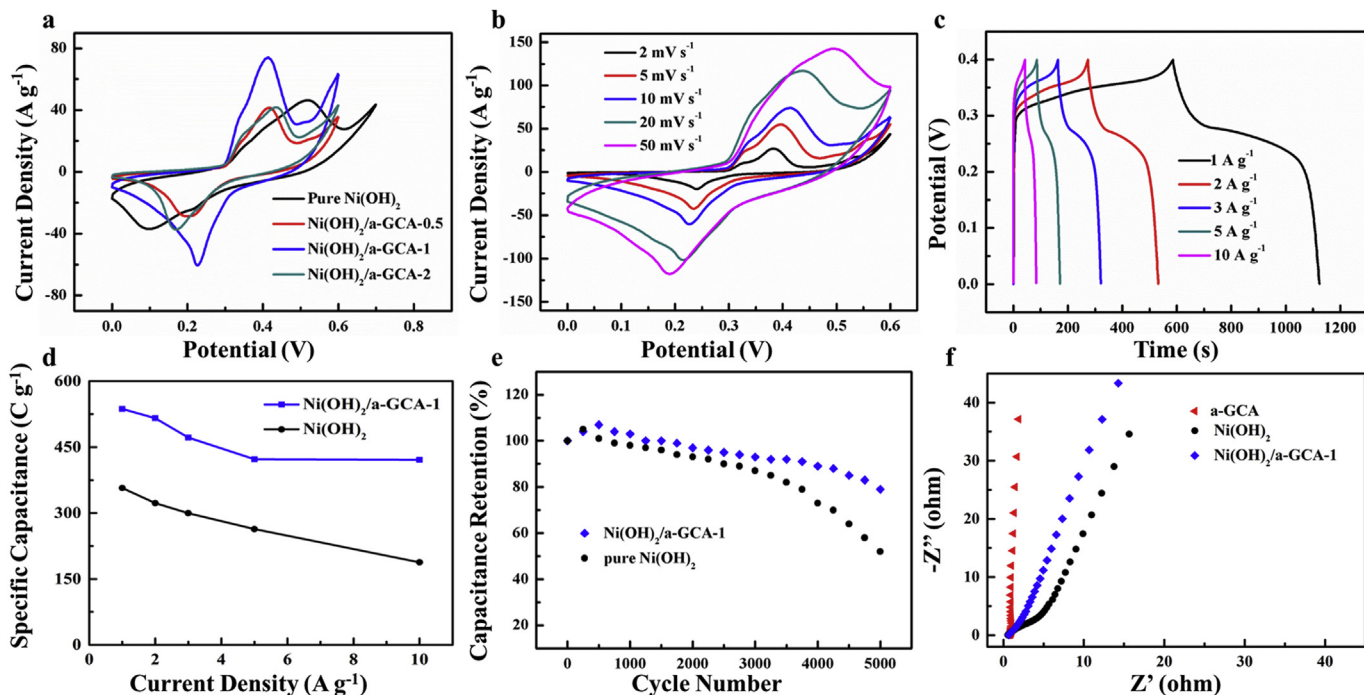
Fig. 6. Electrochemical performance of Ni(OH)$_2$ nanosheets and Ni(OH)$_2$/a-GCA-1 hybrid electrodes with a three-electrode system: (a) CV curves at 10 mV s^{-1}, (b) CV curves of Ni(OH)$_2$/a-GCA-1 at various scan rates, (c) charge/discharge curves of Ni(OH)$_2$/a-GCA-1 at different current densities, (d) rate capability of pure Ni(OH)$_2$, and Ni(OH)$_2$/a-GCA-1 hybrid, (e) cycling stability of pure Ni(OH)$_2$ and Ni(OH)$_2$/a-GCA-1 hybrid upon CV curves at 20 mV s^{-1}, and (f) Nyquist plots for a-GCA, pure Ni(OH)$_2$ and Ni(OH)$_2$/a-GCA-1 hybrid, Z′, real impedance; Z″, imaginary impedance.

pure Ni(OH)$_2$ has poor rate capability. As calculated from the galvanostatic charge/discharge curves in Fig. 6c, the specific capacitances of Ni(OH)$_2$/a-GCA-1 hybrid is 537.0 C g^{-1} at a current density of 1 A g^{-1}. The specific capacitances of pure Ni(OH)$_2$ and Ni(OH)$_2$/a-GCA hybrids at various current densities calculated from the discharge part of galvanostatic charge/discharge curves are summarized in Fig. 6d and Fig. S6d. The specific capacitance of Ni(OH)$_2$/a-GCA-1 hybrid is 421.0 C g^{-1} at a current density of 10 A g^{-1}, which is 78.4% of specific capacitance at a current density of 1 A g^{-1}. While the specific capacitance of pure Ni(OH)$_2$ is 188 C g^{-1} at a current density of 10 A g^{-1}, which is 52.7% of specific capacitance at a current density of 1 A g^{-1}. As for Ni(OH)$_2$/a-GCA-0.5 and Ni(OH)$_2$/a-GCA-2 hybrid, the specific capacitance is 219.0 and 323.0 C g^{-1} at a current density of 10 A g^{-1}, respectively, which is 77.9% and 63.7% of specific capacitance at a current density of 1 A g^{-1}. The remarkably enhanced specific capacitance and rate stability of Ni(OH)$_2$/a-GCA-1 hybrid can be attributed to the following factors. First, carbon skeleton of a-GCA with large surface area offers abundant active sites for in-situ growth of Ni(OH)$_2$ nanosheets, which can well prevent the aggregation of Ni(OH)$_2$ nanosheets. Second, 3D highly porous a-GCA provides interconnected and continuous channels for rapid diffusion of ions and electrons to access the electrochemically active Ni(OH)$_2$ nanosheets for fast Faradaic redox reactions. Besides, the hierarchical pores can buffer the volumetric expansion/contraction of Ni(OH)$_2$ nanosheets at high scan rates and high current densities. Consequently, with a-GCA as template, the Ni(OH)$_2$/a-GCA hybrids show high specific capacitance and good rate stability.

Long term stability is very important for promising supercapacitor materials. The cycling tests for pure Ni(OH)$_2$ and Ni(OH)$_2$/a-GCA-1 were performed by sweeping CV curves at a scan rate of 20 mV s^{-1} for 5000 cycles (Fig. 6e). Clearly, the specific capacitances of pure Ni(OH)$_2$ and Ni(OH)$_2$/a-GCA-1 slightly increased during the first 500 cycles, which can be ascribed to the activation effect which

allows the trapped ions and electrodes gradually diffuse outward. Compared with the 52% retention for pure Ni(OH)$_2$, Ni(OH)$_2$/a-GCA-1 hybrid exhibits 79% retention of capacitance after 5000 cycles, i.e. 0.004% loss of capacitance per cycle. The greatly enhanced cycling stability of Ni(OH)$_2$/a-GCA-1 hybrid can be ascribed to the conductive and porous carbon backbone as buffering substrate to adjust the volumetric expansion/contraction of Ni(OH)$_2$ nanosheets during long term cycling test. EIS was further investigated to analyze the conductive performance, and ion/electrode transport behaviors at the interface between electrolyte and samples. Fig. 6f shows the Nyquist plots of a-GCA, pure Ni(OH)$_2$ and Ni(OH)$_2$/a-GCA-1 hybrid. Clearly, Nyquist plots of a-GCA and Ni(OH)$_2$/a-GCA-1 hybrid exhibit almost no semi-circle in the high frequency region, while that of pure Ni(OH)$_2$ shows a slight quadrant. This demonstrates that the resistance at the electrolyte/electrode interface can be greatly reduced by involving a-GCA. Besides, all samples exhibit straight lines in the low frequency region. Ni(OH)$_2$/a-GCA-1 shows a more vertical line than pure Ni(OH)$_2$, illustrating that the transport resistance of electrons can be greatly decreased with a-GCA used. Consequently, 3D conductive and porous nano-scaffold of a-GCA can shorten the transport path of electrons, and facilitate the diffusion of ions at the electrolyte/electrode interface. Thus, the electrochemical performance can be significantly enhanced for the improved electron transport and fast ion diffusion.

The CV curves of a-GCA measured in KOH electrolyte exhibit the typical rectangular shapes and maintain well from the scan rates of 5 mV s^{-1} to 200 mV s^{-1} (Fig. S7a), indicating that a-GCA has a good electrical double-layer capacitance behavior. Moreover, there are a pair of redox peaks in all CV curves of a-GCA, implying that a-GCA also exhibits pseudocapacitive characteristics, which benefits to improve the capacitance of a-GCA. The specific capacitance calculated from the galvanostatic charge/discharge curves (Fig. S7b) are 361.8, 258.2, 215.0, 199.0 and 190.0 F g^{-1} at 1, 2, 5, 10, 20 A g^{-1}, respectively. The pseudocapacitive behavior is due to the oxygen-

groups on the carbon skeleton, which can be evidenced from the XPS spectra (Fig. S7c and d). The atomic ratios of oxygen element in a-GCA is up to 12.21%. As shown in Fig. 7d, the high resolution C 1s spectrum of a-GCA shows three weak peaks located at 286.7, 287.8, and 288.8 eV, which can be ascribed to -C-O, -C=O, and -COO-, respectively.

The optimized Ni(OH)$_2$/a-GCA-1 hybrid and a-GCA were assembled into a hybrid supercapacitor, where Ni(OH)$_2$/a-GCA-1 applied as positive electrode material and a-GCA used as negative electrode material. This hybrid supercapacitor device was assigned as Ni(OH)$_2$/a-GCA-1//a-GCA. As shown in Fig. 7a, CV curves at the scan rates of 5−100 mV s^{-1} show typical battery-type capacitive behaviors and the curve shapes maintain well even at 100 mV s^{-1}. From the discharge curves, the specific capacitances are 193.7, 164.5, 140.2, 118.4, and 107.6 C g^{-1} at the current densities of 0.8, 1.2, 2.0, 3.2, and 4.0 A g^{-1}, respectively. Moreover, the hybrid supercapacitor shows excellent energy densities of 54.8 and 30.5 Wh kg^{-1} at powder densities of 816 and 4083 W kg^{-1}, respectively. The performance of Ni(OH)$_2$/a-GCA-1//a-GCA is comparable or even better than other Ni(OH)$_2$/carbon-based composites as electrode materials reported previously, which are listed in Table S1. After 5000 cycles, the capacitance of the hybrid supercapacitor still remains 74.8% (Fig. 7c). Furthermore, EIS was investigated to study the electrochemical behavior of Ni(OH)$_2$/a-GCA-1//a-GCA under the rapid diffusion and transfer of ions and charges. As seen in Fig. 7d, there is a tetramolecular circle in the high frequency

region, indicating a solution resistance between the electrolyte and the electrode materials. The solution resistance is about 2.01 Ω. In the low frequency region, the impedance plot is a straight line, showing the good capacitive behavior of this hybrid supercapacitor. Thus, the above electrochemical performance of Ni(OH)$_2$/a-GCA-1//a-GCA hybrid supercapacitor indicates that Ni(OH)$_2$/a-GCA-1 and a-GCA are promising candidates for developing supercapacitors.

To investigate the mechanism for the long-term cyclic stability of Ni(OH)$_2$/a-GCA-1, the electrode was examined by EIS (Fig. 8a) and SEM (Fig. 8b and c) after 5000 cycles. As shown in Fig. 8a, there is also no obvious semicircles in the high frequency region, indicating a high charge transfer rate between the hybrid material and electrolyte. However, compared with EIS curve before cyclic test, the solution resistance is about 1.15 Ω, which is a little higher than that of 0.67 Ω before cyclic test. This may be due to the morphology change during the cyclic test, which hampers the diffusion of electrolyte ions and charges. As can be seen in Fig. 8b and c, after the cycling, nanoparticles, instead of Ni(OH)$_2$ nanosheets, are confined in the a-GCA. This is due to the OH$^-$ intercalation of Ni(OH)$_2$ nanosheets, and the transformation of Ni(OH)$_2$ into NiOOH, as shown in the reaction in equation (5). Because of this reaction, Ni(OH)$_2$ nanosheets are converted to nanoparticles. Besides, the hierarchical porous structures of a-GCA can be clearly observed, suggesting the robust pore walls of a-GCA. Thus, owing to the stable 3D network structure of a-GCA and the excellent confinement effect, Ni(OH)$_2$/a-GCA-1 exhibits good cyclic stability.
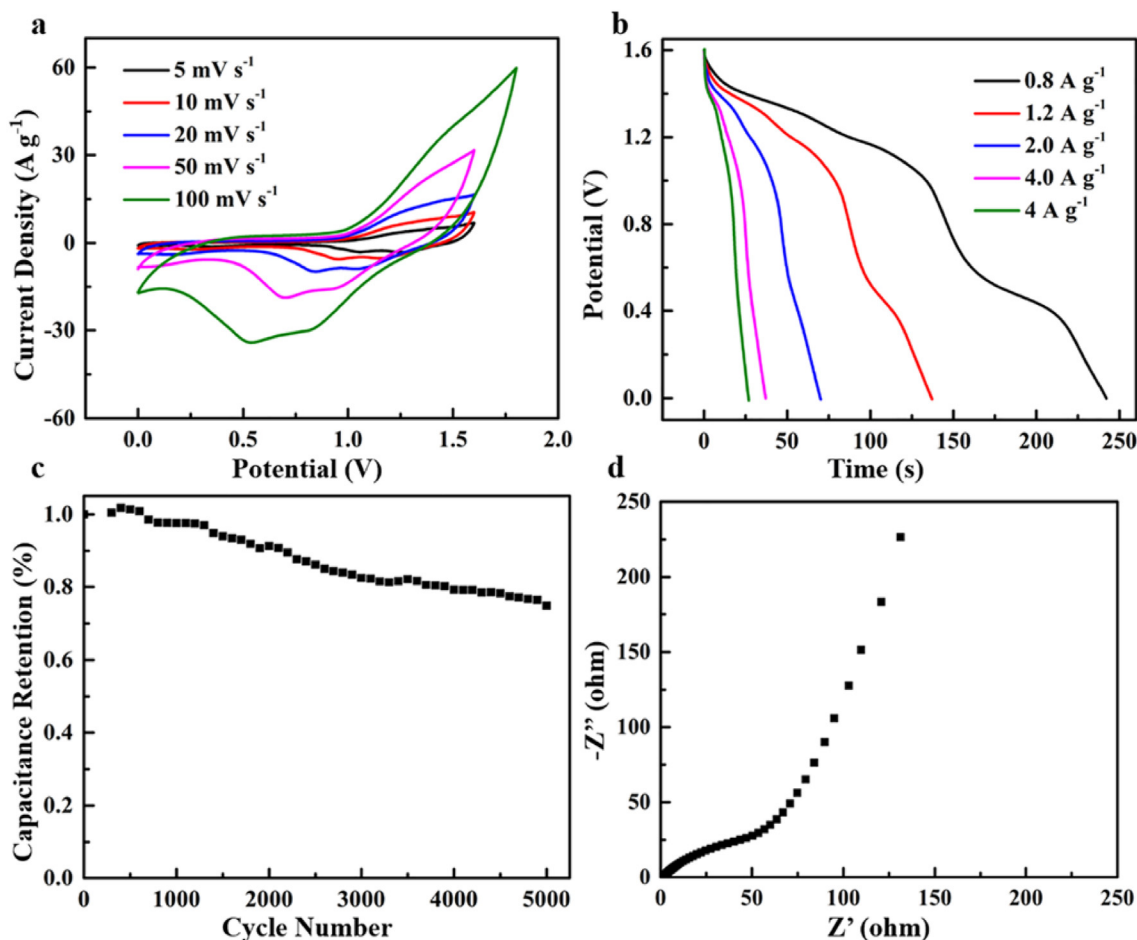

Fig. 7. Electrochemical performance of Ni(OH)$_2$/a-GCA-1//a-GCA hybrid supercapacitor: (a) CV curves at various scan rates, (b) discharge curves at different current densities, (c) cycling stability upon CV curves at 50 mV s^{-1}, and (d) Nyquist plots: Z′, real impedance; Z″, imaginary impedance.
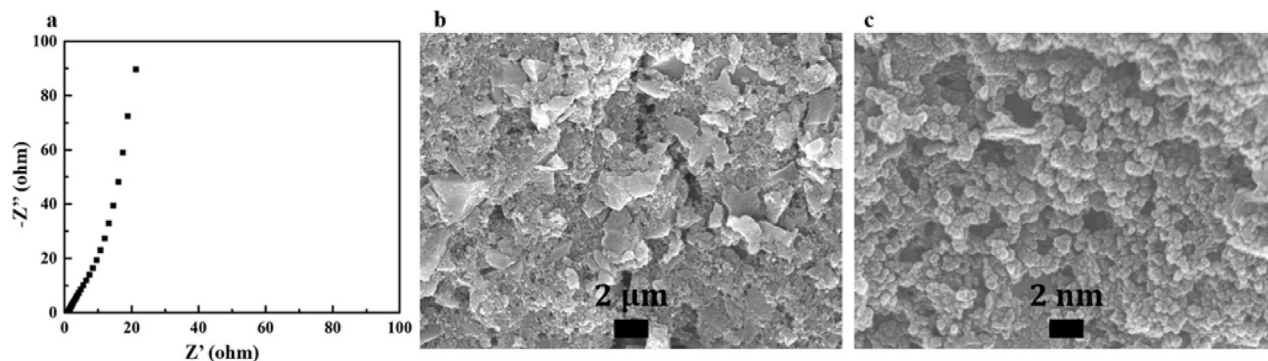
Fig. 8. (a) Nyquist plots, and (b–c) SEM images at low and high magnifications of Ni(OH)$_2$/a-GCA-1 hybrid electrode after cycling for 5000 cycles.

4. Conclusions

In summary, highly porous a-GCA with hierarchical porous structures and large specific surface area has been applied as 3D substrate for in-situ growth of Ni(OH)$_2$ nanosheets without self-aggregation. For the optimized hybrid of Ni(OH)$_2$/a-GCA-1, ultrathin Ni(OH)$_2$ nanosheets are uniformly and vertically anchored on the interconnected and continuous carbon skeleton of a-GCA. Specifically, a-GCA with abundant open multi-level pores (macro-, meso- and micro-pores) provide interpenetrated channels for rapid diffusion of ions and electrons to access Ni(OH)$_2$ nanosheets for fast Faradaic redox reactions, thus enhance the specific capacitance of Ni(OH)$_2$ nanosheets. Besides, the porous structure of a-GCA can buffer the volumetric expansion/contraction of Ni(OH)$_2$ nanosheets during long-term cycling, thus improving the rate and cycling stability of Ni(OH)$_2$ nanosheets. Consequently, the optimized Ni(OH)$_2$/a-GCA hybrid shows a high specific capacitance of 537.0 C g^{-1} at a charge/discharge current density of 1 A g^{-1}, excellent rate capacitance retention of 78.4% at 10 A g^{-1}, and good cyclability of 79% retention after 5000 cycles. Moreover, the assembled Ni(OH)$_2$/a-GCA//a-GCA hybrid supercapacitor device delivers a high energy density of 54.8 Wh kg^{-1} at a powder density of 816 W kg^{-1}. Thus, such an excellent electrochemical performance of Ni(OH)$_2$/a-GCA hybrid makes it promising alternative electrode materials for supercapacitors.

Notes

Acknowledgements

Appendix A. Supplementary data

Supplementary data related to this article can be found at https://doi.org/10.1016/j.electacta.2018.07.043.

References

[1] M. Salanne, B. Rotenberg, K. Naoi, K. Kaneko, P.L. Taberna, C.P. Grey, et al., Efficient storage mechanisms for building better supercapacitors, Nat. Energy 1 (2016) 16070–16080.

[2] A. González, E. Goikolea, J.A. Barrena, R. Mysyk, Review on supercapacitors: technologies and materials, Renew. Sustain. Energy Rev. 58 (2016) 1189–1206.

[3] K. Naoi, W. Naoi, S. Aoyagi, J.I. Miyaoto, T. Kamino, New generation: nano-hybrid supercapacitor, Acc. Chem. Res. 46 (2013) 1075–1083.

[4] M. Daud, M.S. Kamal, F. Shehzad, M.A. Al-Harthi, Graphene/layered double hydroxides nanocomposites: a review of recent progress in synthesis and applications, Carbon 104 (2016) 241–252.

[5] A.M. Abioye, F.N. Ani, Recent development in the production of activated carbon electrodes from agricultural waste biomass for supercapacitors: a review, Renew. Sustain. Energy Rev. 52 (2015) 1282–1293.

[6] A. Borenstein, O. Hanna, R. Attias, S. Luski, T. Brousse, D. Aurbach, Carbon-based composite materials for supercapacitor electrodes: a review, J. Mater. Chem. A 5 (2017) 12653–12672.

[7] F.L. Lai, Y.P. Huang, L.Z. Zuo, H.H. Gu, Y.E. Miao, T.X. Liu, Electrospun nanofiber-supported carbon aerogel as a versatile platform toward asymmetric supercapacitors, J. Mater. Chem. A 4 (2016) 15861–15869.

[8] M. Oschatz, S. Boukhalfa, W. Nickel, J.P. Hofmann, C. Hischer, G. Yushin, et al., Carbide-derived carbon aerogels with tunable pore structure as versatile electrode material in high power supercapacitors, Carbon 113 (2017) 283–291.

[9] X.H. Cao, Y.M. Shi, W.H. Shi, G. Lu, X. Huang, Q.Y. Yan, et al., Preparation of novel 3D graphene networks for supercapacitor applications, Small 7 (2011) 3163–3168.

[10] R.L. Liu, L. Wan, S.Q. Liu, L.X. Pan, D.Q. Wu, D.Y. Zhao, An interface-induced co-assembly approach towards ordered mesoporous carbon/graphene aerogel for high-performance supercapacitors, Adv. Funct. Mater. 25 (2015) 526–533.

[11] Q.Y. Peng, Y.B. Li, X.D. He, X.C. Cui, Y.Y. Shang, C.H. Wang, et al., Graphene nanoribbon aerogels unzipped from carbon nanotube sponges, Adv. Mater. 26 (2014) 3241–3247.

[12] S. Nardecchia, D. Carriazo, M.L. Ferrer, M.C. Gutierrez, F.D. Monte, Three dimensional macroporous architectures and aerogels built of carbon nano-tubes and/or graphene: synthesis and applications, Chem. Soc. Rev. 42 (2012) 794–830.

[13] S.B. Ye, J.C. Feng, P.Y. Wu, Deposition of three-dimensional graphene aerogel on nickel foam as a binder-free supercapacitor electrode, ACS Appl. Mater. Interfaces 5 (2013) 7122–7129.

[14] K.L. Fang, J.Z. Chen, X.Y. Zhou, C.T. Mei, Q.H. Tian, J.L. Xu, et al., Decorating biomass-derived porous carbon with Fe$_2$O$_3$ ultrathin film for high-performance supercapacitors, Electrochim. Acta 261 (2018) 198–205.

[15] Q.Y. Chen, J.Z. Chen, Y.Y. Zhou, C. Song, Q.H. Tian, J.L. Xu, et al., Enhancing pseudocapacitive kinetics of nanostructured MnO$_2$ through anchoring onto biomass-derived porous carbon, Appl. Surf. Sci. 440 (2018) 1027–1036.

[16] Y.F. Zhang, L.Z. Zuo, L.L.S. Zhang, Y.P. Huang, H.Y. Lu, W. Fan, et al., Cotton wool derived carbon fiber aerogel supported few-layered MoSe$_2$ nanosheets as efficient Electrocatalysts for hydrogen evolution, ACS Appl. Mater. Interfaces 8 (2016) 7077–7085.

[17] Y.F. Zhang, W. Fan, Y.P. Huang, C. Zhang, T.X. Liu, Graphene/carbon aerogels derived from graphene crosslinked polyimide as electrode materials for supercapacitors, RSC Adv. 5 (2015) 1301–1308.

[18] Y. Zhou, S.L. Candelaria, Q. Liu, E. Uchaker, G.Z. Cao, Porous carbon with high capacitance and graphitization through controlled addition and removal of sulfur-containing compounds, Nano Energy 12 (2015) 567–577.

[19] Y. Zhou, S.L. Candelaria, Q. Liu, Y.X. Huang, E. Uchaker, G.Z. Cao, Sulfur-rich carbon cryogels for supercapacitors with improved conductivity and wetta-bility, J. Mater. Chem. A 2 (2014) 8472–8482.

[20] Y.F. Zhang, L.Z. Zuo, Y.P. Huang, L.S. Zhang, W. Fan, T.X. Liu, In-situ growth of few-layered MoS$_2$ nanosheets on highly porous carbon aerogel as advanced

electrocatalysts for hydrogen evolution reaction, ACS Sustain. Chem. Eng. 3 (2015) 3140–3148.

[21] Y.F. Zhang, W. Gao, L.Z. Zuo, L.S. Zhang, Y.P. Huang, H.Y. Lu, et al., In situ growth of Fe_2O_3 nanoparticles on highly porous graphene/polyimide-based carbon aerogel nanocomposites for effectively selective detection of dopamine, Adv. Mater. Interfaces 3 (2016) 1600137–1600147.

[22] X.Y. Yao, C.Y. Zhao, J.H. Kong, D. Zhou, X.H. Lu, Polydopamine-assisted synthesis of hollow $NiCo_2O_4$ nanospheres as high-performance lithium ion battery anodes, RSC Adv. 4 (2014) 37928–37933.

[23] Z.Y. Hai, M.K. Akbari, C.Y. Xue, H.Y. Xu, E. Solano, C. Detavernier, et al., Atomically-thin WO_3/TiO_2 heterojunction for supercapacitor electrodes developed by atomic layer deposition, Compos. Commun. 5 (2017) 31–35.

[24] Z.C. Li, J. Han, L. Fan, M.G. Wang, S.Y. Tao, R. Guo, The anion exchange strategy towards mesoporous α-$Ni(OH)_2$ nanowires with multinanocavities for high-performance supercapacitors, Chem. Commun. 51 (2015) 3053–3056.

[25] X.H. Meng, D. Deng, Bio-inspired synthesis of α-$Ni(OH)_2$ nanobristles on various substrates and their applications, J. Mater. Chem. A 4 (2016) 6919–6925.

[26] V.H. Nguyen, C. Lamiel, J.J. Shim, 3D hierarchical mesoporous $NiCo_2S_4$@ $Ni(OH)_2$ core-shell nanosheet arrays for high performance supercapacitors, New J. Chem. 40 (2016) 4810–4817.

[27] F.L. Lai, Y.E. Miao, L.Z. Zuo, H.Y. Lu, Y.P. Huang, T.X. Liu, Biomass-derived nitrogen-doped carbon nanofiber network: a facile template for decoration of ultrathin nickel-cobalt layered double hydroxide nanosheets as high-performance asymmetric supercapacitor electrode, Small 12 (2016) 3235–3244.

[28] S.D. Liu, S.C. Lee, U. Patil, I. Shckery, S. Kang, K. Zhang, et al., Hierarchical MnCo-layered double hydroxides@$Ni(OH)_2$ core-shell heterostructures as advanced electrodes for supercapacitors, J. Mater. Chem. A 5 (2017) 1043–1049.

[29] M.S. Balogun, Y.C. Huang, W.T. Qiu, H. Yang, H.B.Y.X. Tong, Updates on the development of nanostructured transition metal nitrides for electrochemical energy storage and water splitting, Mater. Today 20 (2017) 425–451.

[30] M.S. Balogun, W.T. Qiu, W. Wang, P.P. Fang, X.H. Lu, Y.X. Tong, Recent advances in metal nitrides as high-performance electrode materials for energy storage devices, J. Mater. Chem. A 3 (2015) 1364–1387.

[31] Y. Zhong, X.H. Xia, F. Shi, J.Y. Zhan, J.P. Tu, H.J. Fan, Transition metal carbides and nitrides in energy storage and conversion, Adv. Sci. 3 (2016), 1500286-150314.

[32] M.S. Balogun, Y.X. Zeng, W.T. Qiu, Y. Luo, A. Onasanya, T.K. Olaniyi, Y.X. Tong, Three-dimensional nickel nitride (Ni_3N) nanosheets: free standing and flexible electrodes for lithium ion batteries and supercapacitors, J. Mater. Chem. A 4 (2016) 9844–9849.

[33] A.M. Elshahawy, K.H. Ho, Y.T. Hu, Z. Fan, Y.M. Benndict Hsu, C. Guan, et al., Microwave-assisted hydrothermal synthesis of nanocrystal β-$Ni(OH)_2$ for supercapacitor applications, CrystEngComn 18 (2016) 3256–3264.

[34] H.M. Du, Y.J. Wang, H.T. Yuan, L.F. Jiao, Facile synthesis and high capacitive performance of 3D hierarchical $Ni(OH)_2$ microspheres, Electrochim. Acta 196 (2016) 84–91.

[35] C.L. Wang, H.L. Qu, T. Peng, K.Y. Mei, Y. Qiu, Y. Lu, et al., Large scale α-$Co(OH)_2$ needle arrays grown on carbon nanotube foams as free standing electrodes for supercapacitors, Electrochim. Acta 191 (2016) 133–141.

[36] C.Q. Zhang, Q.D. Chen, H.B. Zhan, Supercapacitors based on reduced graphene oxide nanofibers supported $Ni(OH)_2$ nanoplates with enhanced electrochemical performance, ACS Appl. Mater. Interfaces 8 (2016) 22977–22987.

[37] R.H. Wang, A. Jayakumar, C.H. Xu, J.M. Lee, $Ni(OH)_2$ nanoflowers/graphene hydrogels: a new assembly for supercapacitors, ACS Sustain. Chem. Eng. 4 (2016) 3736–3742.

[38] R.R. Salunkhe, J.J. Lin, V. Malgras, S.X. Dou, J.H. Kim, Y. Yamauchi, Large-scale synthesis of coaxial carbon nanotube/$Ni(OH)_2$ composites for asymmetric supercapacitor application, Nano Energy 11 (2015) 211–218.

[39] Q.Q. He, C. Guan, M.R. Zheng, Y.T. Hu, K.H. Ho, J. Wang, 3D hierarchical SnO_2@ $Ni(OH)_2$ core-shell nanowire arrays on carbon cloth for energy storage application, J. Mater. Chem. A 3 (2015) 9538–9542.

[40] H. Chai, X. Peng, T. Liu, X.H. Su, D.Z. Jia, W.Y. Zhou, High-performance supercapacitors based on conductive graphene combined with $Ni(OH)_2$ nanoflakes, RSC Adv. 7 (2017) 36617–36622.

[41] P. Shen, H.T. Zhang, S.J. Zhang, L.F. Fei, Fabrication of completely interface-engineered $Ni(OH)_2$/rGO nanoarchitectures for high-performance asymmetric supercapacitors, Appl. Surface Sci. (2017). https://doi.org/10.1016/j.apsusc.2017.09.145.

[42] M.K. Liu, W.W. Tjiu, J.S. Pan, C. Zhang, W. Gao, T.X. Liu, One-step synthesis of graphene nanoribbon-MnO_2 hybrids and their all-solid-state asymmetric supercapacitors, Nanoscale 6 (2014) 4233.

[43] M.K. Liu, C. Zhang, W.W. Tjiu, Z. Yang, W.Z. Wang, T.X. Liu, One-step hybridization of graphene nanoribbons with carbon nanotubes and its strong-yet-ductile thermoplastic polyurethane composites, Polymer 54 (2013) 3124–3130.

[44] L. Chen, Y. Hernandez, X.L. Feng, K. Mullen, From nanographene and graphene nanoribbons to graphene sheets: chemical synthesis, Angew. Chem. Int. Ed. 51 (2012) 7640–7654.

[45] D.L. Chao, C.R. Zhu, P.H. Yang, X.H. Xia, J.L. Liu, J. Wang, et al., Array of nanosheets render ultrafast and high-capacity Na-ion storage by tunable pseudocapacitance, Nat. Commun. 7 (2016) 12122–12130.

[46] Y. Gogotsi, R.M. Penner, Energy storage in nanomaterials-capacitive, pseudocapacitive, or battery-like? ACS Nano 12 (2018) 2081–2083.

[47] R.Z. Li, J.P. Liu, Mechanistic investigation of the charge storage process of pseudocapacitive Fe_3O_4 nanorod film, Electrochim. Acta 120 (2014) 52–56.

[48] L.X. Shen, L.H. Du, S.Z. Tan, Z.G. Zang, C.X. Zhao, W.J. Mai, Flexible electrochromic supercapacitor hybrid electrodes based on tungsten oxide films and silver nanowires, Chem. Commun. 52 (2016) 6296–6299.